Breaking the balance of chemical ratio in $ZnAl_2O_4$ to regulate activators and traps for multimode luminescence - A new strategy

Huan Yang[1], Guichang Shen[2], Shuai Tang[2], Ji-Guang Li[3], Qi Zhu[1*]

[1]*Key Laboratory for Anisotropy and Texture of Materials (Ministry of Education), School of Materials Science and Engineering, Northeastern University, Shenyang, Liaoning 110819, PR China*

[2]*State Key Laboratory of Rolling and Automation, Northeastern University, Shenyang 110819, China*

[3]*Research Center for Functional Materials, National Institute for Materials Science, Namiki 1-1, Tsukuba, Ibaraki 305-0044, Japan*

*Corresponding author

Dr. Qi Zhu

Tel: +86-24-8367-2700

E-mail: zhuq@smm.neu.edu.cn

Abstract

As a common transition metal activator, the non-rare earth element Mn has good luminescent properties, so it has been widely concerned. It is reported that Mn^{2+} and Mn^{4+} can coexist in the matrix, and the luminescence of Mn with different valence states is usually controlled by co-doping of other ions. In this work, we controlled the green light emission of Mn^{2+}, the red light emission of Mn^{4+}, and the NIR emission of defects by breaking the balance of chemical ratio in $ZnAl_2O_4$:Mn to achieve multimode luminescence. The spinel-structured $ZnAl_2O_4$ phosphors with deficiency of zinc were synthesized by high temperature solid state reaction, which were characterized by a series of techniques, including XRD, DFT calculation, PLE/PL spectroscopy, TL, persistent luminescence decay curves, and temperature-dependent PL spectra analysis. The deficiency of zinc results in the appearance of zinc vacancy (V_{Zn}) and oxygen vacancy (V_O), and the increased oxygen vacancy defects inhibit the self-reduction of Mn^{4+}. Under the excitation of 325 nm and 426 nm ultraviolet light, the phosphor showed green emission at 510 nm, red emission at 678 nm and near-infrared emission at 767 nm. Due to the increase of vacancy defects, high concentration of zinc deficiency leads to stronger emission of green light, red light and near-infrared light. The phosphor exhibited different light signals at different excitation wavelengths, and the thermal stability of Mn^{2+} and Mn^{4+} luminescence is inconsistent. The above characteristics show that the multimode luminescent phosphor synthesized in this work has broad application prospects in the field of fluorescence anti-counterfeiting.

Keyword: $ZnAl_2O_4$, Mn^{2+}, Mn^{4+}, vacancy defect, multimode luminescence, anti-counterfeiting

1. Introduction

In the field of luminescent materials, non-rare earth element Mn is usually used as activator, because Mn possesses good optical properties and it is cheap and easy to obtain [1]. Therefore, Mn is widely concerned as a good activator. Due to the specific electronic configuration of manganese ion, its luminescence properties also change with the different valence states of manganese ion. Among the valence states of manganese ions, Mn^{2+} and Mn^{4+} are the most common [2]. Mn^{2+} with $3d^5$ electron configuration shows green-light emission in tetrahedral environment (weak crystal field), and Mn^{4+} with $3d^3$ electron configuration shows red-light emission in octahedral environment (strong crystal field) [3]. For example, $Zn_2SiO_4:Mn^{2+}$ [4], $SrAl_2Si_2O_8:Mn^{2+}$ [5], $Cs_2HfF_6:Mn^{4+}$ [6], $K_2SiF_6:Mn^{4+}$ [7] used as green and red phosphors show good luminescence properties. Among them, Mn^{4+} fluoride phosphor showing red-light emission is considered to be used for commercialization because of its high luminous efficiency, which has great application prospects [7]. However, it is challenging to control the valence change of manganese [8]. Moreover, the use of HF as a necessary raw material also greatly limits its application [7, 9, 10]. Therefore, the oxide phosphors doped Mn^{4+} without using hazardous raw materials have received extensive attention.

Mn^{2+} and Mn^{4+} ions can co-exist in some hosts, which may contribute to multimode luminescence. For example, co-doping Mn^{2+} and Mn^{4+} in $Ca_3M_2Ge_3O_{12}$ [11], $LaMgAl_{11}O_{19}$ [3], MgB_2O_4 (B=Al, Ga) [12], $ZnGa_2O_4$ [13], $ZnAl_2O_4$ [14] yielded green and deep red emissions under UV light excitation. Among above hosts, $ZnAl_2O_4$ with broad band gap has a typical spinel structure. In this crystal structure, Zn occupies the tetrahedral site and Al occupies the octahedral site. The structure is classic and there is no reverse defect. $ZnAl_2O_4$ has high chemical and thermal stability, so it is a perfect matrix for metal ions doping [15-17]. Due to the existence of intrinsic defects or defects caused by ion doping in $ZnAl_2O_4$, excessive electrons will be released [18, 19]. This will lead to Mn^{4+} ions transforming to Mn^{2+} ions, which is called as a self-reduction phenomenon. Therefore, the proportion of

Mn^{2+}/Mn^{4+} in the host is uncontrollable [20-23]. Therefore, it is possible to regulate the luminescent properties of phosphors by controlling the self-reduction process of Mn^{4+}. Co-doping ions are frequently used to change the electronic environment in the matrix lattice and thus affecting the proportion of Mn^{2+}/Mn^{4+}. Recently, the molar ratio of Mn^{2+} and Mn^{4+} in $ZnAl_2O_4$ and Mg_2SnO_4 has been adjusted by doping Li^+ to achieve dual-mode luminescence [1, 14, 24]. Usually, co-doping ions with various valence is selected to regulate the electronic environment in the lattice [13, 25]. However, the lattice domain environment becomes complex in presence of new ions. Therefore, it is necessary to explore a simple way for electronic environment regulation.

In addition to cations and anions with fixed lattice positions, there are also some types of defects in the lattice of phosphors, such as vacancies [26]. These defects are often caused by cationic substitution or atomic loss [27]. It is reported that vacancy defects could affect the luminescent properties of phosphors [28, 29]. Recently, it was found that concentration of oxygen vacancy in zinc aluminate could be regulated by the content of zinc deficiency, with the oxygen vacancy acting as the luminescent center, which contributes to near-infrared emission in the range of 650-800 nm [16]. In addition, vacancy defects are not only conducive to the formation of effective hole/electron traps for persistent luminescence, but also can interact with their neighboring ions to adjust their valences [30, 31].

In this work, we prepared $ZnAl_2O_4$ doped Mn ions by a high-temperature solid-state method. Through changing the chemical ratio of $ZnAl_2O_4$, the activators and traps were successfully regulated. The series of phosphors were characterized by XRD, DFT calculation, PLE/PL spectra, persistent luminescence spectra and temperature-dependent PL spectra analysis. The phosphors exhibit multimode luminescence characteristics, indicating they have a prospect in the field of optical anti-counterfeiting.

2. Experiment Section

2.1. Sample preparation

The samples of $ZnAl_2O_4$:*y*Mn (*y* = 0-0.012) and $Zn_{1-x}Al_2O_4$:*y*Mn (*x* = 0-0.13, *y* = 0-0.012) were synthesized by a high temperature solid-state reaction in air atmosphere. The starting materials were Al_2O_3 (99.99%), ZnO (99.99%) and $MnCO_3$ (99.99%). The sources were purchased from China pharmaceutical group chemical reagent Co. LTD (Shanghai, China). Based on the composition, the above materials were weighed stoichio-metrically and mixed homogeneously in an agate mortar. The mixtures were grounded for 30 min homogeneously. After that, the mixtures were pre-fired at 1000 ^oC for 4 h in air. After cooling to room temperature and regrinding for 30 minutes, the samples were sintered at 1500 ^oC for 8 h in air. The heating rate for the two stages of heating is 5 ^oC min^{-1}. Finally, after cooling down to room temperature naturally, $ZnAl_2O_4$:*y*Mn and $Zn_{1-x}Al_2O_4$:*y*Mn phosphors were obtained for further measurement.

2.2. Characterization techniques

X-ray diffractometry (XRD, Model SmartLab, Rigaku, Tokyo, Japan) was employed for phase identification, which was operated at 40 kV/40 mA using nickel-filtered Cu Kα radiation and the data was measured at a speed of 10.0^o 2θ per minute, and the scanning range was 10^o-70^o. The XRD data for Rietveld refinement was gained through the step-scan mode, using a step interval of 0.02 and a counting time of 0.85 s per step. Rietveld refinement was performed using the TOPAS software. Inductively coupled plasma (ICP) spectroscopy (Model Optima 8300 and Optima 4300, Perkin Elmer, Shelton, CT) was employed to analyze the composition of the product with a detection limit of 0.01 wt%. The photoluminescence and persistent luminescence of samples were detected using a JY FL3-21 spectrophotometer (HORIBA) in the spectral range of 200-800 nm at room temperature, and using a slit width of 10 nm in the kinetics mode. The FJ-427A thermoluminescence (TL) instrument (Beijing Nuclear Instrument Factory) was used to measure the TL glow curves. The samples were first exposed to 302 nm UV light for 5 min at room temperature, and the TL glow curves were subsequently recorded from 300 K (27 °C) to 410 K (137 °C) at a heating rate of 1 $K \cdot s^{-1}$.

2.3. Computational Details

Density functional theory (DFT) calculations are carried out using the Vienna ab initio simulation package (VASP) in the study [32]. The electron interaction with ions was replaced by the projector augmented wave (PAW) method, and exchange-correlation potentials between electrons were parameterized by the generalized gradient approximation (GGA) with Perdew–Burke–Ernzerhof (PBE) function [33, 34]. The $3s^2 3p^1$, $3d^{10} 4s^2$ and $2s^2 2p^4$ electrons are the valence electrons of Al, Zn and O, respectively. The tetrahedral and octahedral sites of O were selected as substitution sites. All calculations are performed in 54 atoms without defects. The conjugate-gradient algorithm was used to relax all atomic positions and cell size to achieve the minimum total energy of the systems until the average force on each atom is less than 0.01 eV/atom. The energy cut-off for the plane-wave basis set was kept at a fixed value of 450 eV. The 4 × 4 × 4 k-points mesh obtained by the Monkhorst-Pack method was employed to sample the Brillouin zone [35].

2.4 Preparation of anti-counterfeiting logo

This study used phosphor and aluminum grooves to design multimode fluorescent anti-counterfeit digital patterns. The groove was filled with $Zn_{0.87}Al_2O_4$ and $Zn_{0.87}Al_2O_4$:0.012Mn phosphors. The anti-counterfeit pattern was presented in the form of fluorescent numbers.

3. Result and Discussion

According to the first-principle calculation, the energy of perfect zinc aluminate is determined as -374.157 eV. The energies for Mn atoms to enter tetrahedral and octahedral sites to replace Zn and Al atoms in the zinc aluminate model are shown in Table 1. According to the formula [25, 36, 37]:

$$E(eV) = E_{doped} - E_{prefect} \quad (1)$$

the formation energy of Mn replacing Zn into tetrahedral site is -4.168 eV, and that of Mn replacing Al into octahedral site is -0.353 eV. It can be seen that Mn is more likely to occupy the Zn position when it enters the zinc aluminate lattice.

Table 1. Formation energy of Mn substituting Zn and Al in $ZnAl_2O_4$ lattice.

$ZnAl_2O_4$:Mn	Mn-Zn	Mn-Al
E_D (eV)	-374.51	-378.325
E_F (eV)	-4.168	-0.353

XRD diffraction patterns of $ZnAl_2O_4$:yMn (y = 0-0.012) samples are shown in Figure 1(a). The diffraction positions in the XRD pattern are completely consistent with the PDF standard card of $ZnAl_2O_4$ (JCPDS NO.05-0669). There are no other diffraction peaks, and no obvious diffraction shift is found, indicating that Mn ions were well doped into $ZnAl_2O_4$ lattice to form a homogeneous solid solution. Moreover, with the increase of Mn content, the main lattice of $ZnAl_2O_4$ matrix did not change significantly. Figure 1(b) simulates the atomic site occupation of $ZnAl_2O_4$ lattice doped Mn ions. $ZnAl_2O_4$ is a standard spinel structure, in which Zn occupies tetrahedral position and Al occupies octahedral position [38, 39]. When Mn ions enter the main lattice, both Mn^{2+} and Mn^{4+} ions exist in the crystal cell structure. However, since the ionic radius of Mn^{2+} is 0.66 Å, which is close to that of Zn^{2+} (0.6 Å), Mn^{2+} will preferentially replace Zn^{2+} after entering the lattice and occupy the tetrahedral position. Similarly, the ionic radius of Mn^{4+} is 0.53 Å, which is close to the ionic radius of Al^{3+} ion (0.535 Å), so Mn^{4+} ion preferentially replaces Al^{3+} ion and occupies octahedral position [40, 41].

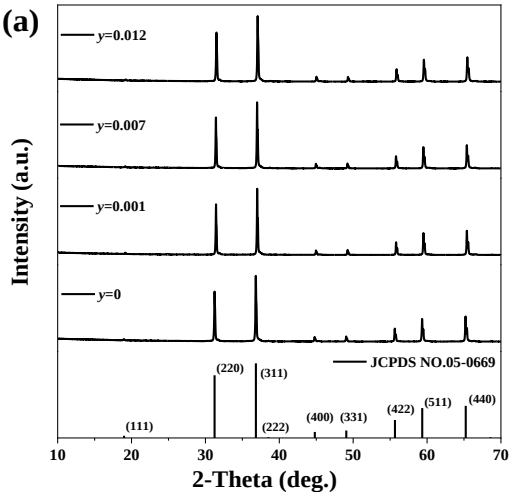

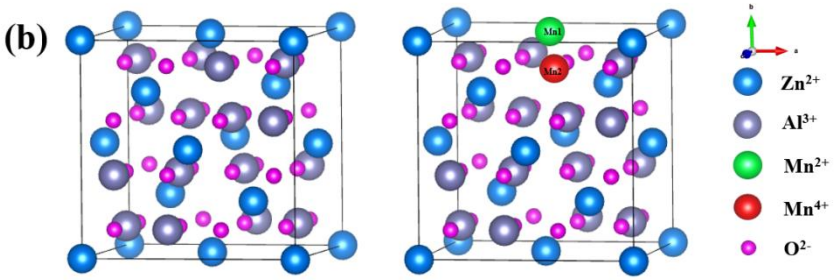

Figure 1. (a) XRD patterns of $ZnAl_2O_4$:*y*Mn (*y* = 0-0.012) calcined at 1500 °C, and (b) the unit cell crystal structure of $ZnAl_2O_4$ and $ZnAl_2O_4$: Mn.

In order to explore the luminescent properties of $ZnAl_2O_4$:*y*Mn phosphors, the series of samples were tested. The samples were monitored by the typical emission wavelength of Mn^{2+} at 510 nm, and the corresponding excitation peaks appeared at 360 nm, 385 nm, 426 nm and 456 nm in PLE spectra (Figure 2(a)). These peaks are corresponding to the $^6A_1$-$^4E(^4D)$, $^6A_1$-$^4T_2$, $^6A_1$-[$^4A_1(^4G)$, $^4E(^4G)$], $^6A_1$-$^4T_1(^4G)$ transitions of Mn^{2+}, respectively [14, 42]. Under the excitation at 426 nm, the sample emits green light at 510 nm (Figure 2(b)), which is assigned to the $^4T_1$-$^6A_1$ transition of Mn^{2+}. With the increase of Mn doping concentration, the green light emission intensity gradually increases, and the optimal doping concentration of Mn^{2+} is *y* = 0.012. However, the PLE spectrum in Figure 2(c) exhibits two obviously wide excitation bands at 325 nm (Mn-O^{2-} CTB) and 456 nm ($^6A_1$-$^4T_1$ transition of Mn^{2+}) by monitoring at 650 nm, indicating there are two different lattice positions of Mn^{2+} in $ZnAl_2O_4$ lattice. It can be recognized from Figures 2(b) and 2(d) that Mn^{2+} ions in two lattice positions can be selectively excited by ultraviolet light of different wavelengths. However, based on the formation energy calculated previously, the formation energy of Mn occupying tetrahedron is lower. Moreover, comparing with the spectral intensity in Figures 2(b) and 2(d), the emission intensity of green light is much higher than that of red light, which further verifies that Mn ion tends to replace Zn^{2+} ion. This is consistent with the first-principles calculation results. It is discovered in Figure 2(d) that under the excitation of 325 nm wavelength, the samples not only display the red emission of Mn^{2+} at 650 nm, but also display the near-infrared emission in the range of 700-800 nm. Through the comparison of PL spectra of

undoped ion sample (y = 0), it is uncovered that the near-infrared emission band has no relationship with Mn doping. It is speculated that it is caused by oxygen vacancy defect in $ZnAl_2O_4$ main lattice, which has been explained in detail in previous work [16]. With the increase of Mn ion concentration, the luminous intensity of the samples increases first and then decreases in Figure 2(d). The quenching concentration of Mn^{2+} ion red light emission is found at y = 0.007. The main reason for concentration quenching is the non-radiative energy transfer between Mn^{2+} ions in the host lattice, which may occur through exchange interaction, radiation reabsorption and multipolar-multipolar interaction [43-45]. When the doping concentration is y = 0.001, the near-infrared light intensity of the sample is the strongest. Therefore, the optimized doping concentration of Mn ion for green light, red light and near-infrared light of the samples is y = 0.012, y = 0.007, and y = 0.001, respectively.

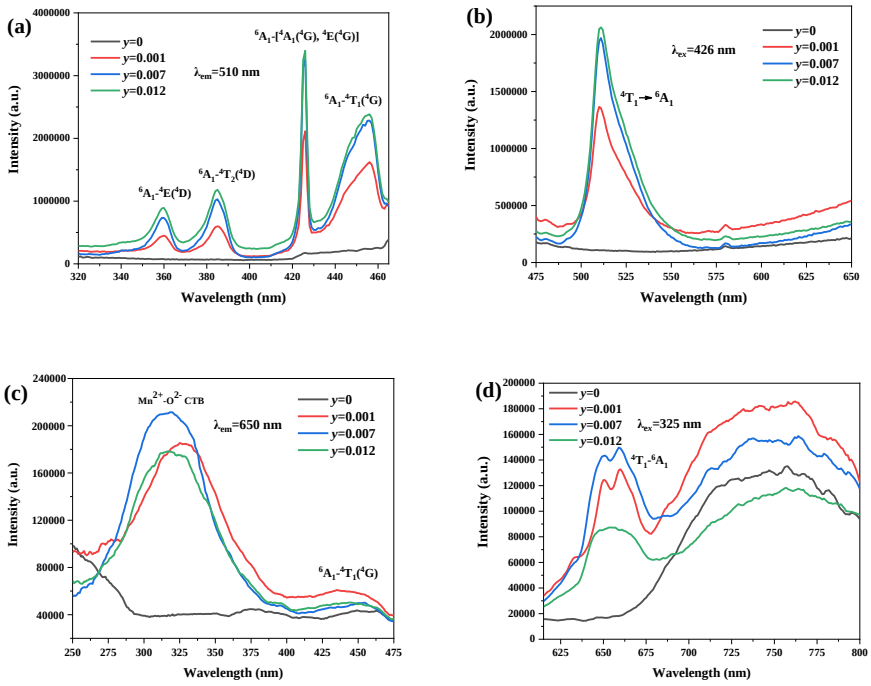

Figure 2. (a, c) PLE and (b, d) PL spectra of $ZnAl_2O_4$:yMn (y = 0-0.012) samples.

In order to investigate the interaction between defects and Mn ions, the samples with different zinc deficiency concentrations were prepared and the XRD diffraction patterns are shown in Figure 3. The XRD diffraction peaks of all samples correspond to the standard card one by one, and the peak positions do not shift significantly, indicating that zinc deficiency did not significantly change the crystal structure of

$ZnAl_2O_4$:Mn. XRD Rietveld refinements for $Zn_{0.87}Al_2O_4$:0.012Mn sample calcined at 1500 ºC is performed using the TOPAS software. The refinement results are shown in Figure S1. The calculation results are consistent with the experimental data. The lattice parameters and the values of R_{wp}, R_p, R_{exp} and χ^2 are provided in the corresponding figure. The values of R_{wp}, R_p and χ^2 are quite low, suggesting that the results are credible. Inductively coupled plasma (ICP) spectroscopy was employed to analyze the composition of the product, and elemental analysis identified the molar ratio of Zn: Al: Mn as 0.85: 1.98: 0.01, which is close to the composition of $Zn_{0.87}Al_2O_4$:0.012Mn. Zinc vacancies will appear in $ZnAl_2O_4$ lattice due to zinc deficiency. However, positively charged oxygen vacancies will also appear for charge balance [16].

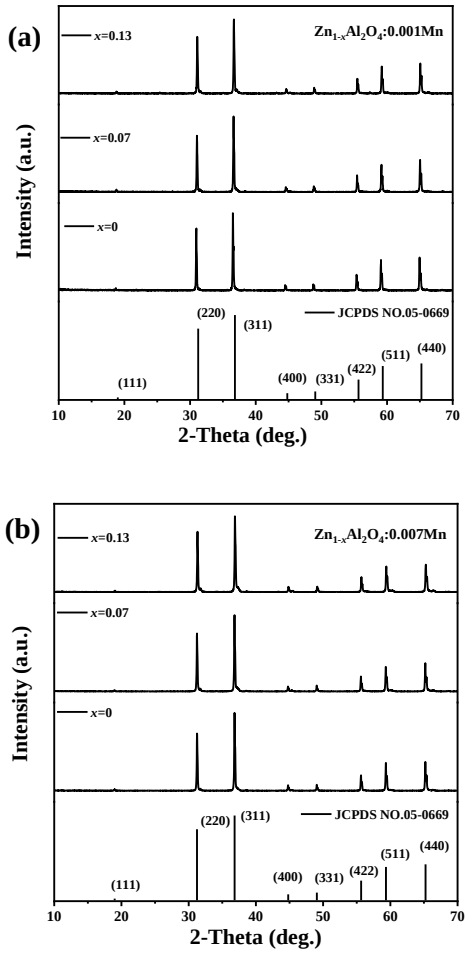

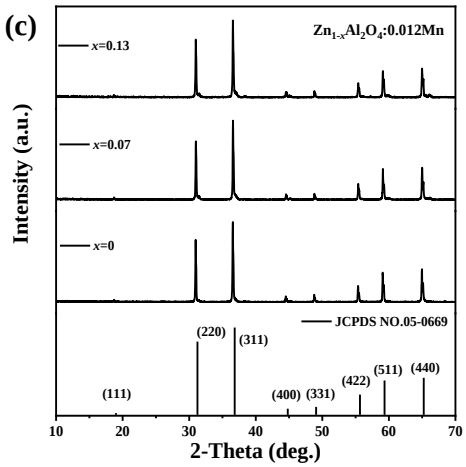

Figure 3. XRD patterns of $Zn_{1-x}Al_2O_4$:Mn (x = 0-0.13) calcined at 1500 °C.

In the PL spectra (Figure 4), it is found that the emission intensity of red light and green light increased gradually with the increase of zinc deficiency concentration, which is consistent with the real-time emissions of samples excited by UV light (insets in Figure 4). The PLE spectra are shown in Figure S2. Because of the zinc vacancies in $ZnAl_2O_4$ lattice due to zinc deficiency, it provides a better opportunity for Mn^{2+} to enter tetrahedral sites easily, which outputs green emission under the activation of ultraviolet light. According to the PL spectrum in Figure 4(b), the samples exhibit two emissions at 650 nm and 767 nm with the x value not larger than 0.07, and the emission intensity increases with x value increasing from 0 to 0.07. However, increasing the x value from 0.07 to 0.13, a new emission peak at 678 nm appears in the PL spectrum, and the emission intensity sharply increases compared to that for x = 0.07 sample. The red light emission at 650 nm is mainly due to the $^4T_1$-$^6A_1$ transition of Mn^{2+}, while the deep red light emission at 678 nm is due to the ^2E-$^4A_2$ energy level transition of Mn^{4+} [21]. When the x value is larger than 0.07, a large number of zinc vacancies appear, accompanied by the generation of many oxygen vacancies, which contributes to the transformation from Mn^{2+} to Mn^{4+} in octahedral environment, thus resulting in deep red emission at 678 nm. In addition, the enhancement of luminescence intensity is due to the oxygen vacancy defects, because they can serve as sensitizers for effective energy transfer to Mn^{2+} and Mn^{4+} [46-48]. When the concentration of zinc deficiency in $Zn_{1-x}Al_2O_4$:Mn phosphor is x = 0, the

oxygen vacancy in the lattice is the intrinsic defect in $ZnAl_2O_4$ lattice. When the concentration of zinc deficiency increased, the oxygen vacancy increased significantly. This also enhances the emission intensity of near-infrared luminescence with defects as the emission center.

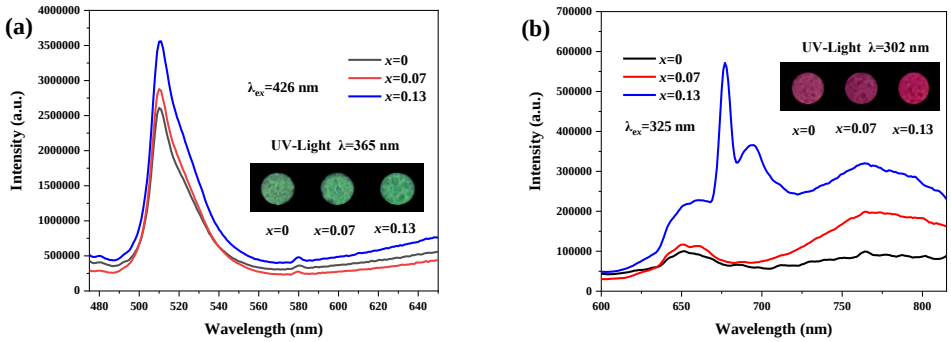

Figure 4. PL spectra of $Zn_{1-x}Al_2O_4$:0.012Mn (x = 0-0.13) samples

Figure 5 shows the PL spectra of samples with various Mn concentrations at the same zinc deficiency concentration (x = 0.13). The emission intensities at 510 nm (Mn^{2+} in tetrahedron site) and 678 nm (Mn^{4+} in octahedron site) all gradually increase at a higher Mn concentration (y value), because of the increased contents of Mn^{2+} in tetrahedron site and Mn^{4+} in octahedron site. However, the strongest red emission at 650 nm and NIR emission at 767 nm are found at y = 0.007 rather than at the largest y value of 0.012. Because Mn^{2+} ions in octahedron site contribute to the emission at 650 nm and oxygen vacancy defects contribute to the emission at 767 nm, there are some Mn^{2+} ions in octahedron site [21]. At a higher Mn content (y value), more Mn^{2+} ions appear in octahedron site, which contributes to more oxygen vacancy defects because of charge balance. Therefore, enhanced emissions at 650 nm and 767 nm are found by increasing the y value from 0.001 to 0.007. But enhanced emission at 678 nm and decreased emissions at 650 nm and 767 nm are found by increasing the y value from 0.007 to 0.012, indicating that further increasing more Mn^{4+} in octahedron site would reduce the number of oxygen vacancy defects and result in the decrease of Mn^{2+} in octahedron site.

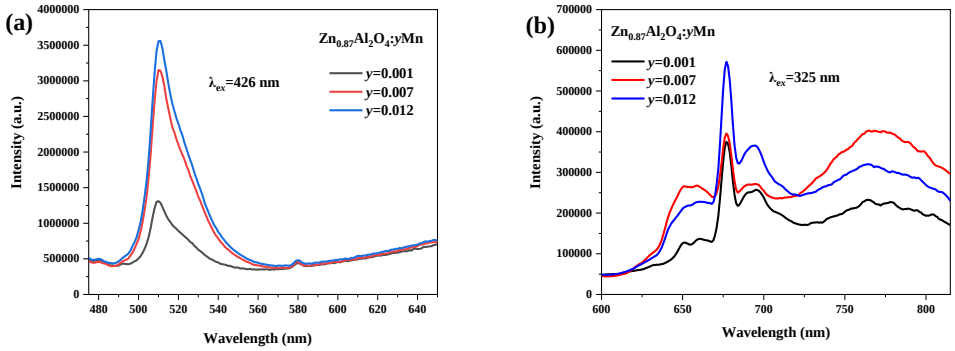

Figure 5. PL spectra of $Zn_{0.87}Al_2O_4$:yMn (y = 0.001-0.012) samples

Figure 6 and Figure S3 show the persistent luminescence decay curves of $Zn_{1-x}Al_2O_4$:0.012Mn (x = 0-0.13) samples after ultraviolet excitation for 5 min. Obviously, the samples exhibit green and deep red afterglows by removing the UV light source (Figure 6), but no obvious NIR afterglow is found (Figure S3). In addition, the zinc deficiency concentration does not significantly affect green afterglow (Figure 6a). But improved deep red afterglow is found at a higher x value, and the x = 0.13 sample shows the best afterglow performance (Figure 6b). The afterglow can last at least for 800 seconds. The electron traps play an important role on afterglow. Under the excitation of ultraviolet light, the traps constantly capture electrons. After stoppage of excitation, due to the influence of thermal disturbance on the electrons in the trap, the electrons will slowly escape from the trap and combine with the excited energy level, thus producing afterglow [49, 50]. The higher the trap concentration, the more electrons trapped and released by the trap, which helps to improve the afterglow [51, 52].

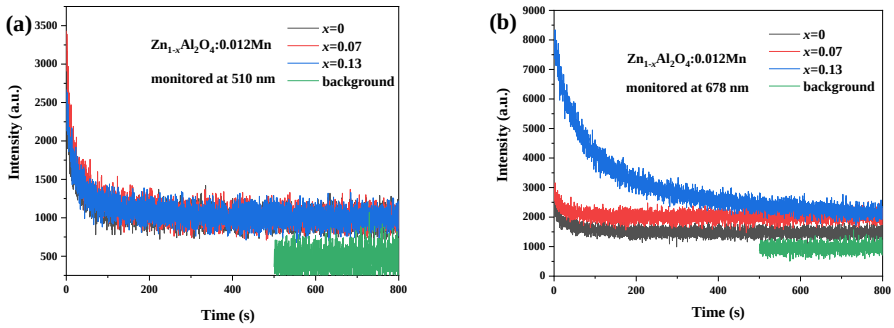

Figure 6. Persistent luminescence decay curves of the $Zn_{1-x}Al_2O_4$:0.012Mn (x = 0-0.13) samples monitored at 510 nm (a) after 365 nm UV light illumination for 5 min, 678 nm (b) after 302 nm

UV light illumination for 5 min.

Shallow traps below 100 ºC are conducive to the occurrence of the afterglow because the electrons they captured can be excited at room temperature [53]. Figure 7 shows the Gaussian fitting TL luminescence curve of the samples, and the approximate trap depth can be estimated by the following formula [51, 54-56]:

$$E = T_m/500 \quad (2)$$

T_m is the Kelvin temperature corresponding to the maximum peak in the TL curve. Figure 7(b-d) show that the fitted spectra of two peaks. The low temperature peak (T_1) and the high temperature peak (T_2) correspond to two shallow traps respectively. These two traps are formed by different defects, and the depth of the electron trap of the sample is shown in Table 2. With the increase of zinc deficiency concentration, it is clear that the concentration of oxygen vacancies traps increases significantly, and the concentration of Mn_{Al}^{+} traps arising from Mn^{4+} replacing Al^{3+} increases slowly. In Table 2, by comparing the peak area ratio of the Gaussian fitting spectra in Figure 7, it is found that the ratio gradually decreases with the increase of zinc deficiency concentration. Therefore, it speculates that T_1 corresponds to Mn_{Al}^{+} trap and T_2 corresponds to Vo trap. As shown in Figure 6, the green afterglow intensity monitored at 510 nm did not significantly increase with the change of defect concentration, while the red afterglow intensity monitored at 678 nm gradually increased with the increase of defect concentration. With the increase of zinc vacancy, the depth of oxygen vacancy trap decreases from 0.756 eV to 0.73 eV, and electrons are easier to be released. However, the $^4T_1$ energy level of Mn^{4+} is located below the conduction band, and the $^4T_1$ energy level is closer to the conduction band comparing with the ^4E energy level of Mn^{2+}, so electrons relaxed to the $^4T_1$ excited state energy level can be preferentially accepted. Therefore, with more defects, the red afterglow of Mn^{4+} gradually increases, while the green afterglow intensity of Mn^{2+} almost remains unchanged.

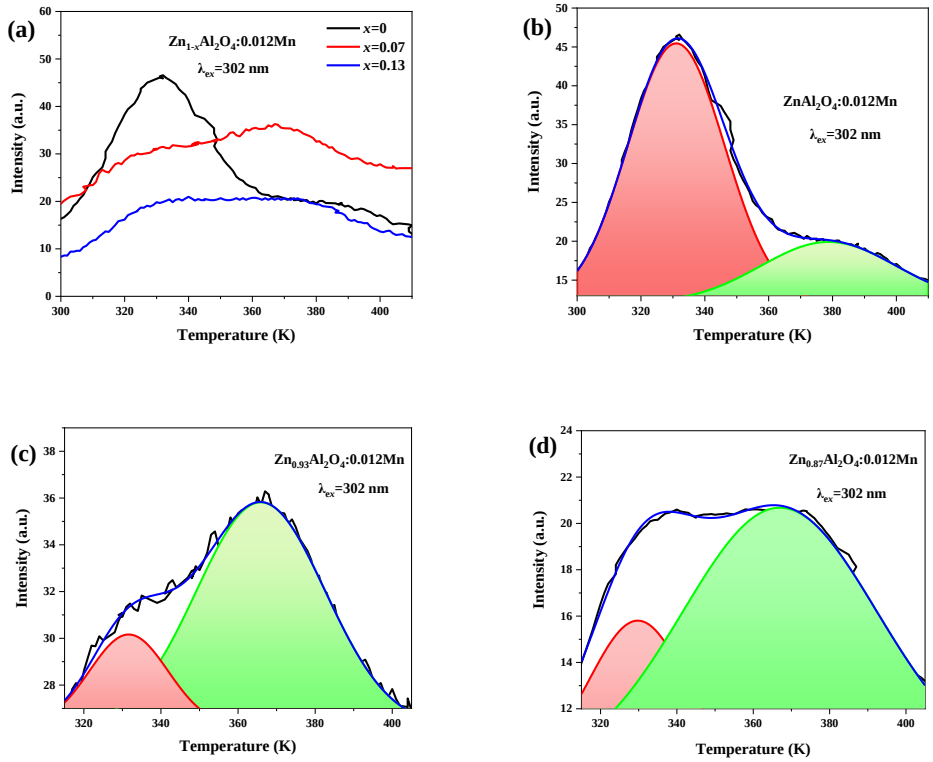

Figure 7. (a) Thermo-luminescence (TL) curves of $Zn_{1-x}Al_2O_4$:0.012Mn (x = 0-0.13), gaussian fitting spectra of (b) $ZnAl_2O_4$:0.012Mn, (c) $Zn_{0.93}Al_2O_4$:0.012Mn and (d) $Zn_{0.87}Al_2O_4$:0.012Mn samples excited at 302 nm.

The energy level splitting of Mn^{2+} in tetrahedral and octahedral coordination environment and Mn^{4+} in octahedral coordination environment can be represented by Tanabe-Sugano energy level diagram, as shown in Figures 8(a) and 8(b). In order to explore the luminescence mechanism of Mn^{2+} and Mn^{4+} in $Zn_{1-x}Al_2O_4$:yMn, the mechanism diagram is speculated combining with the Tanabe-Sugano energy diagram, as shown in Figure 8(c).

Table 2 $Zn_{1-x}Al_2O_4$: 0.012Mn (x = 0-0.13) trap depth and TL fitting peak area ratio

$Zn_{1-x}Al_2O_4$:0.012Mn	T_1	T_2	E_1	E_2	Peak area ratio (A_1/A_2)
x = 0	332 K	378 K	0.664 eV	0.756 eV	3.025
x = 0.07	331 K	367 K	0.662 eV	0.734 eV	0.2863
x = 0.13	331 K	365 K	0.662 eV	0.730 eV	0.2574

Under the excitation of ultraviolet light, the electrons of Mn^{2+} in tetrahedral site undergo $^6A_1$-^4E, $^6A_1$-$^4T_2$, $^6A_1$-$^4A_1$, $^6A_1$-$^4T_1$ energy level transitions, then are transferred to the $^4T_1$ level via non-radiative relaxation, and finally returned to the $^6A_1$ state with green light output. Mn^{2+} in octahedral coordination environment emit red

light after undergoing this process. The electrons of Mn^{4+} in $ZnAl_2O_4$:*y*Mn are excited from the ground state level $^4A_2$ to the excited state levels $^4T_2$, $^2T_2$, $^4T_1$ and Mn^{4+}-O^{2-} charge transfer energy band, then are transferred to the ^2E level via non-radiative relaxation, and finally returned to the $^4A_2$ state with an excellent red light output. In addition, due to the existence of V_{Zn} and V_O traps in the sample, 325 nm ultraviolet light can excite the electrons from the V_{Zn} level to the V_O level and conduction band and leave holes in the V_{Zn} level. Among them, the electrons excited to the V_O level return to the V_{Zn} level through non-radiative transition and recombine with the holes to form the electron-hole pairs, thus realizing the emission of near-infrared light [16]. However, the electrons excited to the conduction band will be trapped by V_O traps and Mn_{Al}^+ traps. After stopping the excitation, the electrons will slowly release from the trap and relax to the excited energy levels of Mn^{2+} and Mn^{4+} and finally contribute to the red and green afterglow of Mn^{2+} and Mn^{4+}.

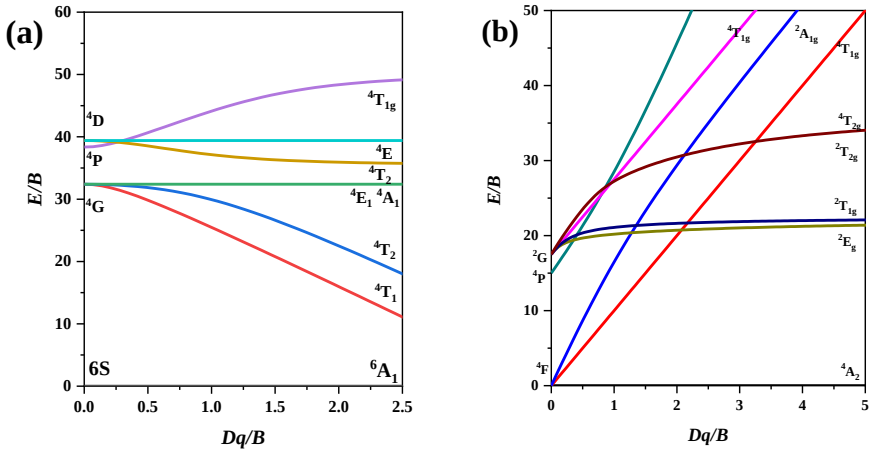

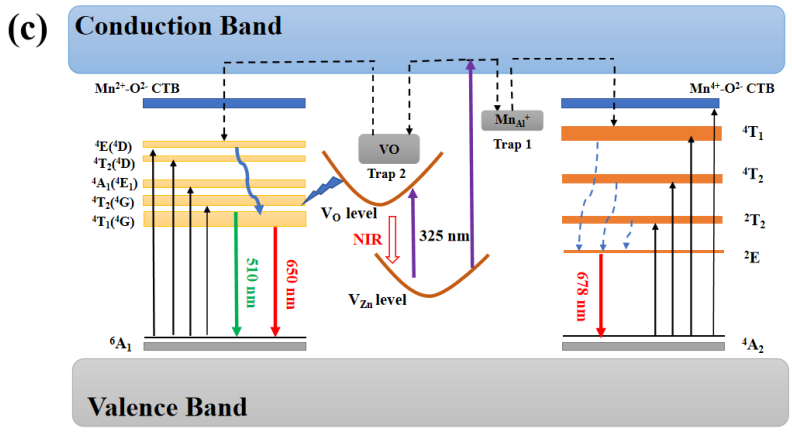

Figure 8. Tanabe-Sugano spectra of Mn^{2+} (a) and Mn^{4+} (b) ions, (c) luminescence mechanism diagram of $Zn_{1-x}Al_2O_4$:yMn.

Figure 9 shows the varied emission intensity of the samples at different temperatures under different excitation wavelengths. With the increase of temperature, the decrease of luminous intensity is due to the enhancement of molecular thermal motion at high temperature, which intensifies the non-radiative transition [57]. When the sample is excited by ultraviolet light, the electrons of Mn^{2+} and Mn^{4+} are pumped from the ground state level to the excited state level, and then fall back to the ground state level to realize the emission of red and green light. In addition, some electrons are trapped by electron traps (Vo and Mn_{Al}^{+} traps). In the process of thermal excitation, although the electrons in the shallow electron trap are greatly consumed, the electrons in the deep electron trap are easily released under thermal disturbance [58-59]. Because the deep electron trap is closer to the Mn^{2+} energy level, the tunneling effect between the oxygen vacancy level and the Mn^{2+} energy level results in more electrons accumulating at the excited state level of Mn^{2+} [60]. With the increase of heating temperature, although the luminous intensity of the sample decreases gradually, the increase of temperature promotes the release of electrons from the trap to compensate for the emission loss [61]. Therefore, when the temperature rises to 125 ºC, the luminous intensity of Mn^{2+} can still reach 79.17% of that at room temperature. However, the luminous intensity of Mn^{4+} is relatively low (58.36%) at 125 ºC.

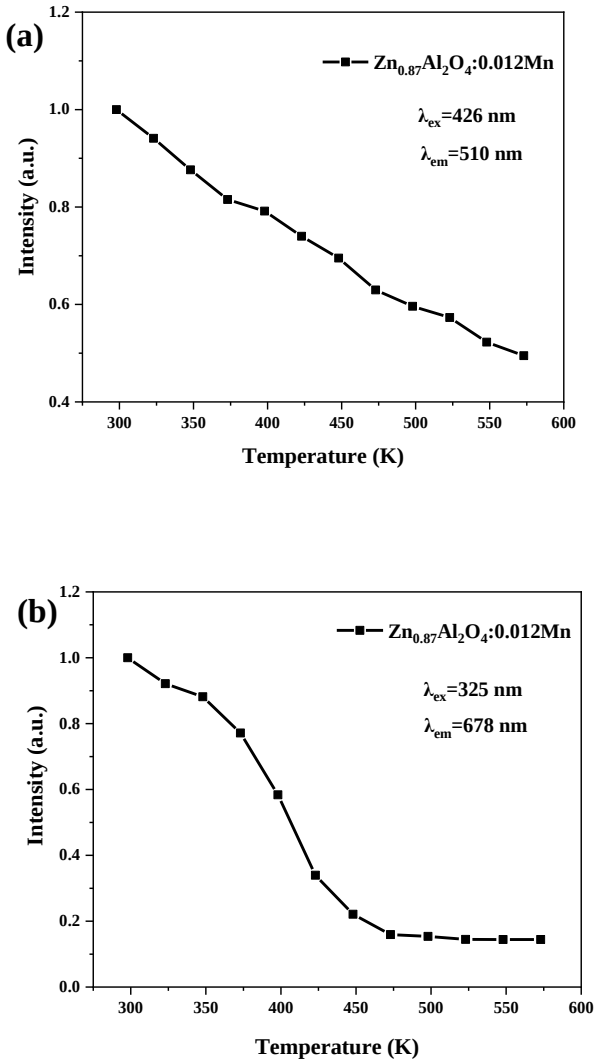

Figure 9. Temperature-dependent emission intensities of 510 nm and 678 nm for $Zn_{0.87}Al_2O_4$:0.012Mn sample excited at (a) 426 nm and (b) 325 nm.

Figure 10(a) shows the appearance of $Zn_{1-x}Al_2O_4$:0.012Mn (x = 0-0.13) samples at different heating temperatures with different excitation wavelengths. Obviously, when the temperature rises to 498 K, the sample still maintains intense green and near-infrared light, but there is almost no red light. Based on the luminescence characteristics and thermal stability of the samples, multimode anti-counterfeiting application using $Zn_{0.87}Al_2O_4$ and $Zn_{0.87}Al_2O_4$:0.012Mn as component is shown in Figure 10(b). $Zn_{0.87}Al_2O_4$ phosphor only emits near-infrared light, while $Zn_{0.87}Al_2O_4$:0.012Mn phosphor emits green light, red light and near-infrared light. The phosphors were filled into the designed aluminum groove template with “370”

number as the correct password pattern. First, under the irradiation of different wavelengths of ultraviolet light (365 nm and 302 nm), the phosphors showed green visible light and red visible light of “370” at room temperature, respectively. However, the pattern under 302 nm ultraviolet light showed near-infrared “898” number, using night vision instrument. Another anti-counterfeiting method is to use the thermal stability of the sample to verify the correct digital pattern. When the sample was heated to 225 °C, the green visible light “370” excited by 365 nm ultraviolet light still kept an intense signal, but the red visible light “370” excited by 302 nm is almost invisible. It can be seen that the multimode luminescence phosphors have a potential application in the field of fluorescence anti-counterfeiting.

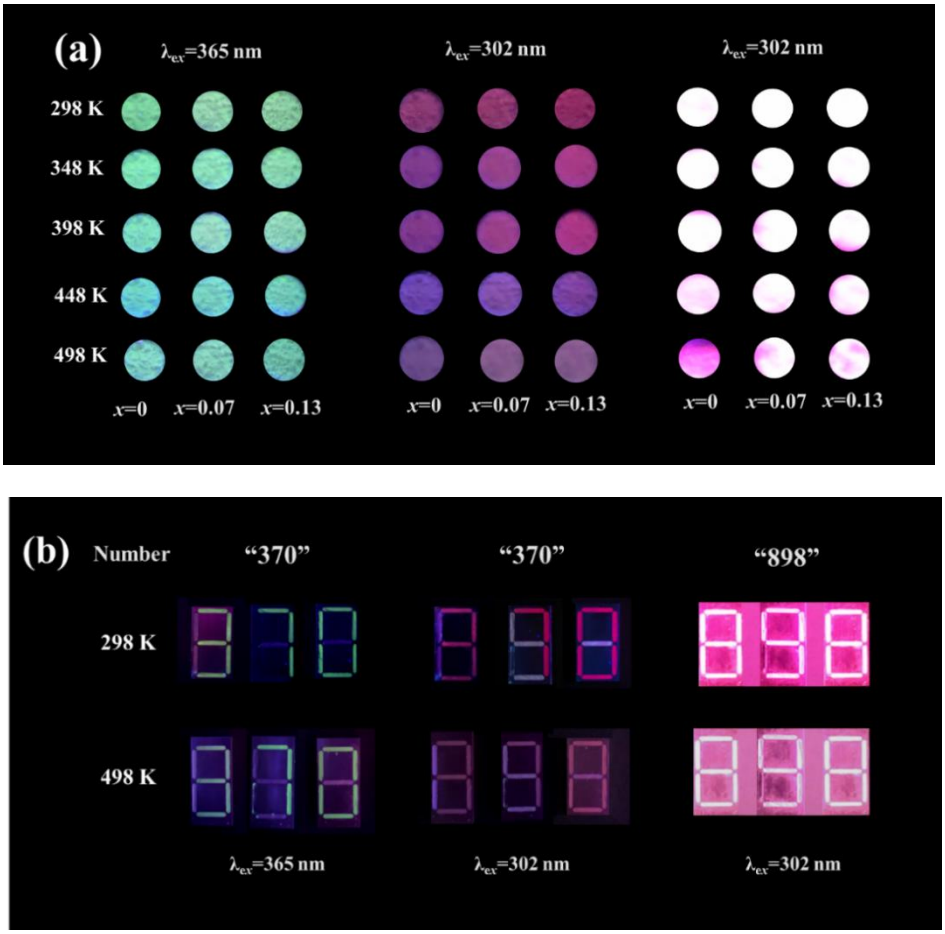

Figure 10. (a) Appearance of $Zn_{1-x}Al_2O_4$:0.012Mn (x = 0-0.13) samples at different temperatures, (b) digital demonstration of multimode anti-counterfeiting logo using $Zn_{0.87}Al_2O_4$ and $Zn_{0.87}Al_2O_4$:0.012Mn phosphors.

4. Conclusion

$Zn_{1-x}Al_2O_4$:yMn (x = 0-0.13, y = 0-0.012) phosphors were synthesized by a high temperature solid state reaction, which were characterized by a series of techniques, including XRD, DFT calculation, PLE/PL spectroscopy, TL, persistent luminescence decay curves, and temperature-dependent PL spectra analysis. In this spinel solid solution, Mn^{2+} and Mn^{4+} ions replace the tetrahedral position (Zn position) and octahedral position (Al position), respectively. They emit 510 nm green light with afterglow ($^4T_1$ (G)-$^6A_1$ (S) transition of Mn^{2+}) and 678 nm red light with afterglow (^2E-$^4A_2$ transition of Mn^{4+}). The introduction of vacancy defects does not significantly affect the crystal structure. Increasing the value of x leads to more zinc vacancies and oxygen vacancies, and vacancy defects inhibit the self-reduction of Mn^{4+} ions at the Al site, providing more opportunities for Mn^{2+} ions to occupy the Zn position. The introduction of vacancy defects effectively regulates the emission centers of Mn^{2+} and Mn^{4+} in $ZnAl_2O_4$. The increase of vacancy defects can not only induce enhanced near-infrared emission at 767 nm, but also improve green emission at 510 nm and red emission at 678 nm. The prepared samples show multimode luminescence behavior by changing the excitation wavelength, indicating that they are the potential materials in application of advanced optical anti-counterfeiting.

Conflicts of interest

The authors declare that they have no conflict of interest.

Acknowledgments

This work was supported in part by the Fundamental Research Funds for the Central Universities (Grant N2302004) and National Natural Science Foundation of China (Grants 51302032, U21A2045, 52172112).

References and Notes

[1] J.P. Xue, T. Hu, F.Q. Li, F.W. Liu, H. M. Noh, B.R. Lee, B.C. Choi, S. Park, J.H. Jeong, P. Du, Suppressed self-reduction of manganese in Mg_2SnO_4 via Li^+ incorporation with polychromatic luminescence for versatile applications, Laser Photonics Rev. 17 (2023) 2200832.

[2] A. Banerjee, Y. Shilina, B. Ziv, J. M. Ziegelbauer, S. Luski, D. Aurbach, I. C.Halalay, On the oxidation state of manganese ions in Li-ion battery electrolytesolutions, J. Am. Chem. Soc. 139 (2017) 1738-1741.

[3] D.Y. Huang, Q.Y. Ouyang, B. Liu, B.K. Chen, Y.T. Wang, C.G. Yuan, H. Xiao, H.Z. Lian, J. Lin, Mn^{2+}/Mn^{4+} co-doped $LaM_{1-x}Al_{11-y}O_{19}$ (M=Mg, Zn) luminescent materials: electronic structure, energy transfer and optical thermometric properties, Dalton Trans. 50 (2021) 4651.

[4] C. Barthou, J. Benoit, P. Benalloul, Mn^{2+} concentration effect on the optical properties of Zn_2SiO_4:Mn phosphors, J. Electrochem. Soc. 141 (1994) 524-528.

[5] B. Wang, Y.C. Kong, Z. K. Chen, X. S. Li, S. P. Wang, Q. G. Zeng, Thermal stability and photoluminescence of Mn^{2+} activated green-emitting feldspar phosphor $SrAl_2Si_2O_8:Mn^{2+}$ for wide gamut w-LED backlight, Opt. Mater. 99 (2019) 109535.

[6] T. Senden, E.J.V. Harten and A. Meijerink, Synthesis and narrow red luminescence of $Cs_2HfF_6:Mn^{4+}$, a new phosphor for warm white LEDs, J. Lumin. 194 (2017) 131-138.

[7] L. Huang, Y. Liu, J. B. Yu, Y.W. Zhu, F. J. Pan, T.T. Xuan, M.G. Brik, C.X. Wang, J. Wang, Highly stable $K_2SiF_6:Mn^{4+}@K_2SiF_6$ composite phosphor with narrow red emission for white LEDs, ACS Appl. Mater. Interfaces 10 (2018) 18082-18092.

[8] Y. Arai, S. Adachi, Optical properties of Mn^{4+}-activated Na_2SnF_6 and Cs_2SnF_6 red phosphors, J. Lumin. 131 (2011) 2652-2660.

[9] S. Adachi, T. Takahashi, Direct synthesis and properties of $K_2SiF_6:Mn^{4+}$ phosphor by wet chemical etching of Si wafer, J. Appl. Phys. 104 (2008) 317.

[10] Y.H. Kim, J. Ha, W.B. Im, Towards green synthesis of Mn^{4+}-doped fluoride phosphors: a review, J. Mater. Res. Technol. 11 (2021) 181-195.

[11] L.P. Dong, L. Zhang, Y.C. Jia, B.Q. Shao, W. Lü, S. Zhao, H.P. You, Site occupation and luminescence of novel orange-red $Ca_3M_2Ge_3O_{12}$:Mn^{2+}, Mn^{4+} (M = Al, Ga) phosphors, ACS Sustainable Chem. Eng. 8 (2020) 3357-3366.

[12] Y. Wakui, Y.J. Shan, K. Tezuka, H. Imoto, M. Ando, Crystal-site engineering approach for preparation of MgB_2O_4:Mn^{2+}, Mn^{4+} (B = Al, Ga) phosphors: control of green/red luminescence properties, Mater. Res. Bull. 90 (2017) 51-58.

[13] T. Si, Q. Zhu, J.Q. Xiahou, X.D. Sun, and J.G. Li, Regulating Mn^{2+}/Mn^{4+} activators in $ZnGa_2O_4$ via Mg^{2+}/Ge^{4+} doping to generate multimode luminescence for advanced anti-counterfeiting, ACS Applied Electronic Materials, ACS Appl. Electron. Mater. 3 (2021) 2005-2016.

[14] Y.B. Chen, J.Q. Chen, J.H. Liang, J. He, Z.Q. Liu, Y.D. Yin, Localized charge accumulation driven by Li^+ incorporation for efficient LED phosphors with tunable photoluminescence, Chem. Mater. 32 (2020) 9551-9559.

[15] M.T. Tran, D.Q. Trung, N. Tu, D.D. Anh, L.T.H. Thu, N.V. Du, N.V. Quang, N.T. Huyen, N.D.T. Kien, D.X. Viet, N.D. Hung, P.T. Huy, Single-phase far-red-emitting $ZnAl_2O_4$:Cr^{3+} phosphor for application in plant growth LEDs, J. Alloys Compd. 884 (2021) 161077.

[16] H. Yang, J.Q. Xiahou, Q. Zhu, J.G. Li, Considerable improved near-infrared luminescence in ionic-free doped $ZnAl_2O_4$ by oxygen defects engineering, J. Lumin. 253 (2023) 119455.

[17] H. Dixit, N. Tandon, S. Cottenier, R. Saniz, D. Lamoen, B. Partoens, First-principles study of possible shallow donors in $ZnAl_2O_4$ spinel, Phys. Rev. B 87 (2013) 174101.

[18] J.Q. Hu, E.H. Song, S. Ye, B. Zhou, Q.Y. Zhang, Anomalous spontaneous-reduction of Mn^{7+}/Mn^{4+} to Mn^{2+} and luminescence properties in Zn_2GeO_4:Mn, J. Mater. Chem. C 00 (2013) 1-3.

[19] H.M. Chen, L.W. Wu, F. Bo, J.K. Jian, L. Wu, H.W. Zhang, L.R. Zheng, Y.F.

Kong, Y. Zhang, J.J. Xu, Coexistence of self-reduction from Mn^{4+} to Mn^{2+} and elastico-mechano luminescence in diphase $KZn(PO_3)_3:Mn^{2+}$, J. Mater. Chem. C 7 (2019) 7096.

[20] L. Dong, L. Zhang, Y. Jia, B. Shao, W. Lu, S. Zhao, H. You, Site occupation and luminescence of novel orange-red $Ca_3M_2Ge_3O_{12}:Mn^{2+}$, Mn^{4+} (M = Al, Ga) phosphors. ACS Sustainable Chem. Eng. 8 (2020) 3357-3366.

[21] L. Dong, L. Zhang, Y. Jia, B. Shao, W. Lu, S. Zhao, H. You, Enhancing luminescence and controlling the Mn valence state of $Gd_3Ga_{5-x-\delta}Al_{x-y+\delta}O_{12}:y$Mn phosphors by the design of the garnet structure. ACS Appl. Mater. Interfaces 12 (2020) 7334-7344.

[22] J. Hu, E. Song, S. Ye, B. Zhou, Q. Zhang, Anomalous spontaneous-reduction of Mn^{7+}/Mn^{4+} to Mn^{2+} and luminescence properties in Zn_2GeO_4:Mn. J. Mater. Chem. C 5 (2017) 3343-3351.

[23] J. Hu, E. Song, Y. Zhou, S. Zhang, S. Ye, Z. Xia, Q. Zhang, Non-stoichiometric defect-controlled reduction toward mixed-valence Mn-doped hexaaluminates and their optical applications. J. Mater. Chem. C 7 (2019) 5716-5723.

[24] J.G. Cheng, P.L. Li, Z.J. Wang, Z.L. Li, M.M. Tian, C. Wang, Z.P. Yang, Color selective manipulation in $Li_2ZnGe_3O_8:Mn^{2+}$ by multiple-cations substitution on different crystal-sites, Dalton Trans. 47 (2018) 4293-4300.

[25] H.C Sun, Q. Zhu, J.G. Li, Local charge regulation by doping Li^+ in $BaGa_2O_4:Bi^{3+}$ to generate multimode luminescence for advanced optical morse code, Ceram. Int. 48 (2022) 9640-9650.

[26] V Lisitsyn, L Lisitsyna, E Polisadova, Nanodefect substructures in crystal phosphors, Mater. Sci. Eng. 81 (2015) 012020.

[27] X.D. Lu, W.G. Shu, Roles of crystal defects in the persistent luminescence of Eu^{2+}, Dy^{3+} co-doped strontium aluminate based phosphors, Rare Met. 26 (2007) 305.

[28] T. Selvalakshmi, S. Sellaiyan, A. Uedono, T. Semba, A. C. Bose, Investigation on photoluminescence properties and defect chemistry of $GdAlO_3:Dy^{3+}$, Ba^{2+}

phosphors, Opt. Mater. 58 (2016) 524-530.

[29] Z.H. Ju, R.P. Wei, J.R. Zheng, X.P. Gao, S.H. Zhang, Synthesis and phosphorescence mechanism of a reddish orange emissive long afterglow phosphor Sm^{3+}-doped Ca_2SnO_4, Appl. Phys. Lett. 98 (2011) 121906.

[30] H. Duan, Y.Z. Dong, Y. Huang, Y.H. Hu, X.S. Chen, First-principles study of intrinsic vacancy defects in $Sr_2MgSi_2O_7$ phosphorescent host material, J. Phys. D: Appl. Phys. 49 (2016) 025304.

[31] Y. Wei, H. Yang, Z.Y. Gao, X.H. Yun, G.C. Xing, C.G. Zhou, G.G. Li, Anti-thermal-quenching Bi^{3+} luminescence in a cyan-emitting $Ba_2ZnGe_2O_7$:Bi phosphor based on zinc vacancy. Laser & Photonics Rev. 15 (2021) 2000048.

[32] G. Kresse, J. Furthmuller, Efficient iterative schemes for ab initio total-energy calculations using a plane-wave basis set, Phys. Rev. B 54 (1996) 1116.

[33] P.E. Blochl, Projector augmented-wave method, Phys. Rev. B 50 (1994) 17953.

[34] J.P. Perdew, K. Burke, M. Ernzerhof, Generalized gradient approximation made simple, Phys. Rev. Lett. 77 (1996) 3865.

[35] G.C. Shen, L.X. Li, S. Tang, J.F. Jin, X.J. Chen, Q. Peng, Stability and elasticity of quasi-hexagonal fullerene monolayer from first-principles study, Crystals 13 (2023) 224.

[36] C.X. Yang, T.Y. Liu, Z.J. Cheng, H.X. Gan, J.Y. Chen, Study on Mn-doped $SrTiO_3$ with first principle calculation, Phys. B 407 (2012) 844-8480.

[37] S. Huang, J.G. Li, X. Wang, Q. Zhu, X. Sun, Controlled synthesis and the effects of Gd^{3+} substitution, calcination, and particle size on photoluminescence of $(Y_{0.95-x}Gd_xTb_{0.05})_2O_3$ green phosphor spheres. Chem. Eng. J. 306 (2016) 322-329.

[38] S. Pin, M. Suardelli, F. D. Acapito, G. Spinolo, M. Zema, S. C. Tarantino, P. Ghigna, Role of interfacial energy and crystallographic orientation on the mechanism of the $ZnO + Al_2O_3 \rightarrow ZnAl_2O_4$ solid-state reaction: I. reactivity of films deposited onto the sapphire (110) and (012) faces, J. Phys. Chem. C 117 (2013) 6105-6112.

[39] Q. Lu, Z.Q. Wei, X.J. Wu, S.P. Huang, M.J. Ding, J.H. Ma, Electronic structure

and optical properties of spinel structure $Zn_{1-x}Ni_xAl_2O_4$ nanopowders synthesized by sol-gel method, Chem. Phys. Lett. 772 (2021) 138582.

[40] X.Y. Sun, Z. He, X. Gu, Persistent luminescence of $Zn_2GeO_4:Mn^{2+}/Pr^{3+}$ phosphors, J. Mater. Sci.: Mater. Electron. 29 (2018) 17217-17221.

[41] G.X. Li, G. Li, Q.N. Mao, L. P., H. Yu, M.J. Liu, L. Chu, J.S. Zhong, Efficient luminescence lifetime thermometry with enhanced Mn^{4+}-activated $BaLaCa_{1-x}Mg_xSbO_6$ red phosphors, Chem. Eng. J. 430 (2022) 132923.

[42] Q. Zhou, L. Dolgov, A.M. Srivastava, L. Zhou, Z.L. Wang, J.X. Shi, M.D. Dramicánin, M.G. Brik, M.M. Wu, Mn^{2+} and Mn^{4+} red phosphors: synthesis, luminescence and applications in WLEDs. J. Mater. Chem. C 6 (2018) 2652.

[43] D. L. Dexter, J. H. Schulman, Theory of concentration quenching in inorganic phosphors, J. Chem. Phys. 22 (1954) 1063.

[44] T. Senden, R.J.A. Dijk-Moes, A. Meijerink, Quenching of the red Mn^{4+} luminescence in Mn^{4+}-doped fluoride LED phosphors, Light: Sci. Appl. 7 (2018) 8.

[45] R.R. Cui, X. Guo, X.Y. Gong, C.Y. Deng, Photoluminescence properties and energy transfer of novel orange-red emitting phosphors: $Ba_3Bi_2(PO_4)_4:Sm^{3+}$, Eu^{3+} for white light-emitting diodes, Rare Met. 40 (2021) 2882-2891.

[46] J.Q. Long, X.Y. Yuan, C.Y. Ma, M.M. Du, X.L. Ma, Z.C. Wen, R. Ma, Y.Z. Wang, Y.G. Cao, Strongly enhanced luminescence of $Sr_4Al_{14}O_{25}:Mn^{4+}$ phosphor by co-doping B^{3+} and Na^+ ions with red emission for plant growth LEDs, RSC Adv. 8 (2018) 1469-1476.

[47] X.X. Xu, Y.H. Wang, Y. Gong, W. Zeng, Y.Q. Li, Effect of oxygen vacancies on the red phosphorescence of $Sr_2SnO_4:Sm^{3+}$ phosphor, Opt. Express, 18 (2010) 16989-16994.

[48] W.W. Ji, M.H. Lee, L.Y. Hao, X. Xu, S. Agathopoulos, D.W. Zheng, C.H. Fang, Role of oxygen vacancy on the photoluminescence of $BaMgSiO_4$:Eu phosphors: experimental and theoretical analysis, Inorg. Chem. 54 (2015) 1556-1562.

[49] Y.X. Zhuang, J. Ueda, S. Tanabe, Tunable trap depth in $Zn(Ga_{1-x}Al_x)_2O_4$:Cr, Bi

red persistent phosphors: considerations of high-temperature persistent luminescence and photostimulated persistent luminescence, J. Mater. Chem. C 1 (2013) 7849.

[50] T. Maldiney, A. Bessière, J. Seguin, E. T. Eston, S. K. Sharma, B. Viana, A.J.J. Bos, P. Dorenbos, M. Bessodes, D. Gourier, D. Scherman1, C. Richard, The in vivo activation of persistent nanophosphors for optical imaging of vascularization, tumours and grafted cells, Nat. Mater. 13 (2014) 418-426.

[51] H.J. Guo, W.B. Chen, W. Zeng, G. Li, Y.H. Wang, Y.Y. Li, Y. Li, X. Ding, Structure and luminescent properties of a novel yellow super long lasting phosphate phosphor $Ca_6BaP_4O_{17}:Eu^{2+}$, Ho^{3+}, J. Mater. Chem. C 3 (2015) 5844-5850.

[52] X.M. Teng, W.D. Zhuang, H.Q. He, Influence of La^{3+} and Dy^{3+} on the properties of the long afterglow phosphor $CaAl_2O_4:Eu^{2+}$, Nd^{3+}, Rare Met. 27 (2008) 335.

[53] L. Xi, L. Pan, Y. Wang, P.D. Townsend, The influence of doped Cr ions on the luminescence properties of infrared long persistent phosphor $ZnAl_2O_4$ with the substitution of Ge ions, J. Lumin. 233 (2021) 117941.

[54] R. Chen, Glow curves with general order kinetics, J. Electrochem. Soc. 116 (1969) 1254.

[55] Z.Z. Wang, Z. Song, L.X. Ning, Z.G. Xia, Q.L. Liu, Enhanced yellow persistent luminescence in $Sr_3SiO_5:Eu^{2+}$ through Ge incorporation, Inorg. Chem. 58 (2019) 8694-8701.

[56] R. Chen, On the calculation of activation energies and frequency factors from glow curves, J. Appl. Phys. 40 (1969) 2.

[57] Y.H. Guo, S.H. Zhou, X.K. Sun, X.D. Lao, H.L. Yuan, $BaAl_{12}O_{19}:Eu^{2+}$ phosphors: molten salt flux synthesis and blue emission with high color purity and excellently thermal stability, J. Lumin. 211 (2019) 271-275.

[58] J. Ueda, S. Miyano, S. Tanabe, Formation of deep electron trap by Yb^{3+} codoping leads into super-long persistent luminescence in Ce^{3+}-doped yttrium aluminum gallium garnet phosphors, ACS Appl. Mater. Interfaces 10 (2018) 20652-20660.

[59] W.X. Wang, J.X. Yang, Z.H. Zou, J.C. Zhang, H.H. Li, Y.H. Wang, An isolated deep-trap phosphor for optical data storage, Ceram. Int. 44 (2018) 10010-10014.

[60] R. Pang, W.Z. Sun, J.P. Fu, H.F. Li, Y.L. Jia, D. Li, L.H. Jiang, S. Zhang, C.Y. Li, Luminescence properties of a novel reddish orange long-lasting phosphorescence phosphor $Zn_2P_2O_7$:Sm^{3+}, Li^+, RSC Adv. 5 (2015) 82704-82710.

[61] J.R. Du, A. Feng, D. Poelman, Temperature dependency of trap-controlled persistent luminescence, Laser Photonics Rev. 14 (2020) 2000060.

Graphic Abstract